



An articulated spine and ribcage kinematic model for simulation of scoliosis deformities

Hamed Shayestehpour¹ · John Rasmussen¹ · Pavel Galibarov² · Christian Wong³

Received: 9 September 2020 / Accepted: 9 March 2021 / Published online: 30 March 2021
© The Author(s), under exclusive licence to Springer Nature B.V. 2021

Abstract Musculoskeletal multibody modeling can offer valuable insight into aetiopathogenesis behind adolescent idiopathic scoliosis, which has remained unclear. However, the underlying model should represent anatomical joints with compatible kinematic constraints while allowing the model to attain scoliotic postures. This work presents an improved and kinematically determinate model including the whole spine and ribcage, which can attain typical scoliosis deformations of the thorax with compatible constraint strategy and simulate the interaction between all the bony segments of the ribcage and the spine. In the model, costovertebral/costotransverse joints were defined as universal joints based on reported anatomical studies. Articulations between ribs and the sternum were defined as spherical joints except in the ninth and tenth pairs, which have one additional anteroposterior degree-of-freedom. The model is controlled by 15 kinematic parameters, including spinal rhythms and parameters relating to clinical metrics of scoliosis. These input values were measured from the bi-planar radiographs of a 17-year-old scoliosis patient with a right main thoracic curve of 33° Cobb angle. Dependent kinematic variables with clinical relevance were selected for validation purposes and compared with measurements from radiographs. The average errors of rib-vertebra angles, rib-vertebra angle differences, and rib humps were 6.6° and 9.0°, and 6.3 mm. The model appeared to reproduce the spine and rib deformation pattern conforming to radiographs, results in simulating the rib prominence, rib spread, rib-vertebra angles, and sternum orientation, therefore supporting the constraint definitions. The model can subsequently be used to investigate the kinetics of scoliosis and contribute to uncovering the pathomechanism.

Keywords Thoracolumbar spine · Multibody modeling · Ribcage kinematics · Compatible joint definition · Scoliosis · AnyBody

✉ H. Shayestehpour
hs@mp.aau.dk

¹ Department of Materials and Production, Aalborg University, Aalborg East, Denmark

² AnyBody Technology A/S, Aalborg, Denmark

³ Department of Orthopedics, University Hospital of Hvidovre, Hvidovre, Denmark

1 Introduction

Scoliosis is a complex three-dimensional deformation of the spine. Adolescent Idiopathic Scoliosis (AIS) is the most common form of it. Despite several studies to unravel the aetiologies and pathogeneses that underlie AIS [1–4], the aetiopathogenesis behind AIS has remained unclear [2–4]. We hypothesize that musculoskeletal multibody modeling can offer valuable insight into the matter. Therefore, we extend recently published thoracolumbar models with a kinematically consistent ribcage to obtain a model that can plausibly represent the biomechanics of the system.

Most of the models to investigate the biomechanics of the trunk have used the finite element method [5]; some to model the spine alone [6–9], and some to include the ribcage system [10–12]. However, despite the critical role of the trunk musculature in kinetics and stability of the spine [13–16], most of the finite element models have excluded muscle contraction and considered muscles as purely passive elements. A few finite element models include some active muscles [17–20]. Multibody models can simulate the movements and muscle actions of the living spine at a modest computational cost. They are also able to simulate the kinematics of the spine in separation from kinetics [5]. Additionally, multibody models allow the combination of independently developed models into the system, providing the opportunity to easily add a spine model into a whole-body model and allow the different parts to interact with each other and transfer loads through joints without changing the boundary conditions [21].

Most of the multibody spine models have been devoted to the lumbar region, where the thorax has been considered as a single rigid body, or the mechanical contribution of the ribcage has been neglected [22–28], which possibly leads to inaccurate representations of spine biomechanics. Some prior models include an articulated thoracic spine, but neglect the contribution of the ribcage or the comprehensive thoracic musculature [29–33] or have represented the ribcage's effects from its stiffness properties only [34]. However, studies and clinical observations indicate that the kinematic constraints of the thoracic bony components play an important role in thoracic stability and force transmission [34–36], and this notion also influences clinical practice because radiographic observations of skeletal displacements form the basis of diagnostics and treatment in the field. A model including the kinematics of the ribcage is therefore required for a comprehensive understanding of the biomechanics of the thoracolumbar spine.

A few detailed musculoskeletal models of the entire thoracolumbar spine with articulated ribcage have been proposed to estimate *in vivo* skeletal and muscular loads during dynamic activities [37–40], and they represent the current state-of-the-art in the field, from which the present work began. They can reconstruct spine deformations, albeit with kinematically indeterminate constraint strategies. The kinematic constraints of the joints form the boundary conditions for the equilibrium equations, from which muscle forces and joint reactions can be derived, so they are essential for a valid mechanical representation of the system. Constraint assumptions can be evaluated through kinematically admissible deformation states, their compatibility with anatomical joint properties, and ability to represent experimentally observed deformations. In other words, model constraint definitions should be compatible with the anatomical joints while allowing the model to attain scoliotic postures.

This task is complicated because the chain of links forming the human thorax contains multiple closed loops, which make its kinematic constraints nontrivial, especially in the presence of pathological deformations, which tend to cause locking in models with redundant kinematic constraints. We, therefore, assume that compatible joint kinematics is a necessary condition for correct biomechanics and ultimately for obtaining an understanding of the pathomechanism of AIS.

This work presents an improved and kinematically determinate model, which can attain typical scoliosis deformations of the thorax and simulate the interaction between all the bony segments of the ribcage and the spine. The model consists of multiple closed loops corresponding to the ribcage, comprising rigid bodies interconnected with different types of joints.

2 Methods

2.1 The kinematic spine model

The model was created using the AnyBody™ Modeling System v. 7.2 (AnyBody Technology, Aalborg, Denmark), which is a software system for three-dimensional multibody dynamics simulation [41]. The system uses a Cartesian formulation [42] to form a mathematical model based on constraint definitions and solves the position problem from the nonlinear constraint equations. The constraints originate from the user's definition of joints and from kinematic drivers, which can be any holonomic measure of kinematics, e.g. angles, distances between segments, and various mathematical combinations of them. In contrast to joint constraints, the values of drivers can change during the simulation to form different postures and spine curves [41]. The model is kinematically determinate when the system of nonlinear equations formed by constraints and drivers is solvable. This usually entails equal numbers of degrees-of-freedom (DOFs) and constraint equations.

The previously presented lumbar [28] and cervical spine models [43], together with a thoracolumbar spine model with articulated ribcage [38] form the basis for the development of the new multibody spine model. Individual rigid osseous elements are already defined within these regions. They comprise pelvis, sacrum, five lumbar vertebrae, twelve thoracic vertebrae, ten pairs of ribs (the floating ribs were fixed to their vertebrae), the sternum, seven bony segments of the cervical region, and the skull. In the current development, the pelvis is grounded with a one-component revolute joint allowing lateral rotation, but the model can be connected to the lower extremity models to form a full body. In the following, we describe joint definitions that render the model kinematically determinate in concert with clinically meaningful driver definitions.

2.1.1 Joint definitions

Intervertebral discs in the entire spine were defined as spherical joints. The centers of the intervertebral joints of the lumbar region were defined from previous work [44]. For the thoracic region, the location of the centers was defined as 65% posterior to the middle of the space between the upper and lower endplates, similar to the lumbar joints definition. The center of the cervical joints lies in the middle of the space between the endplates of the discs.

The articulation between ribs and vertebrae is constrained by the costovertebral (CV) and costotransverse (CT) joints (CVCTJ). In previous work [37–40], they are implemented as a single compound revolute joint or a single spherical joint. However, with the coordinate definition by Lemosse et al. [45], *in vitro* experimental investigation shows that the range-of-motion of the rib rotations in two directions dominate the third direction [45, 46]. Therefore, a rational assumption is to disregard rotation about the latter axis. Besides, Beyer et al. [47] have published results from *in vivo* breathing analysis implying that the rib rotations in two

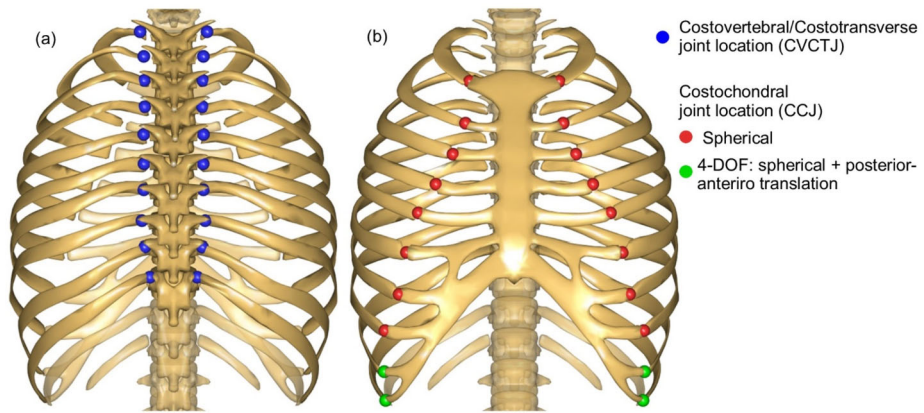


Fig. 1 (a) The rotation centers of the costovertebral/costotransverse joints (CVCTJ) from the posterior view (blue nodes). (b) The centers of the costochondral joints (CCJ) from the anterior view, spherical joints (red nodes), and four-DOFs joints allowing three-DOFs rotation and one-DOF anterior-posterior translation (green nodes) (Color figure online)

directions are greater than the third direction with a slightly different coordinate system definition, which supports the aforementioned assumption.

In this model, the CVCTJ complex was modeled as a compound universal joint, allowing rotation in two directions, based on the following assumptions: The CV joints were assumed as spherical joints allowing for three independent rotations. The CT joints are assumed to provide one additional constraint preventing separation of the rib perpendicularly to the facet surface, which prevents rib rotation about the longitudinal axis of the joint. Together, these assumptions result in two rotational DOFs for the CVCTJ complex, which is the definition of a universal joint. This definition also corresponds to the aforementioned assumption that arises from *in vivo* and *in vitro* analysis on clinical data of intact ribs [45–47].

In this work, the origin of the CVCTJ coordinate system was placed in the rotational center of the articular surface of the CV joint (Fig. 1(a)). The axis directions of the joint coordinate system (Fig. 2(a)) were defined by rotation from the global coordinate system (x -axis posterior-anterior, y -axis longitudinal, z -axis mediolateral) by 20° about the y -axis followed by 5° about the z -axis. These angles were selected to align the X_{CVCT} -axis with the axis from the CT to CV facets. The Z_{CVCT} -axis is the normal vector from the articular facet of the transverse process (similar to the Y -axis of Lemosse et al. [45]), and the Y_{CVCT} -axis is perpendicular to the X_{CVCT} and Z_{CVCT} axes. This definition allows for the personalization of the CVCTJ coordinate system if the CV and CT are detectable from medical imaging. Figure 2(b) shows the resulting DOFs of the CVCTJ complex with rotations about X_{CVCT} and Z_{CVCT} . Finally, individual kyphosis angles were assigned to each vertebra to form the shape of the thoracic spine in the sagittal plane in the standing posture (Fig. 3).

To define the articulations between the ribs and the sternum, i.e. the costochondral joints (CCJ), the sternum, and the costal cartilages were assumed as one rigid body. The CCJs were defined as spherical joints for all ribs, except the ninth and tenth pairs, which were modeled as four-DOFs trans-spherical joints allowing three rotations and one anterior-posterior translation. We assumed that the lower deformable costal cartilages have greater length, therefore more mobile cartilaginous junctions compared to other pairs of ribs [48] (Fig. 1(b)).

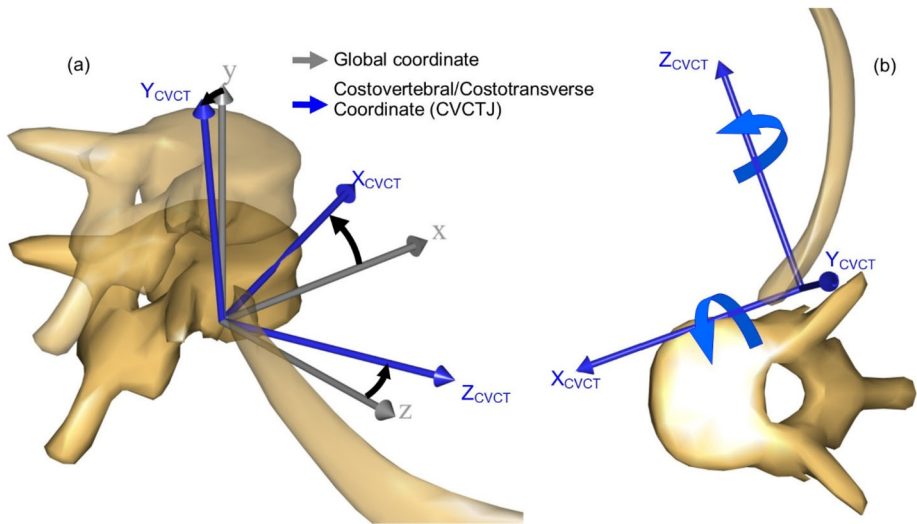
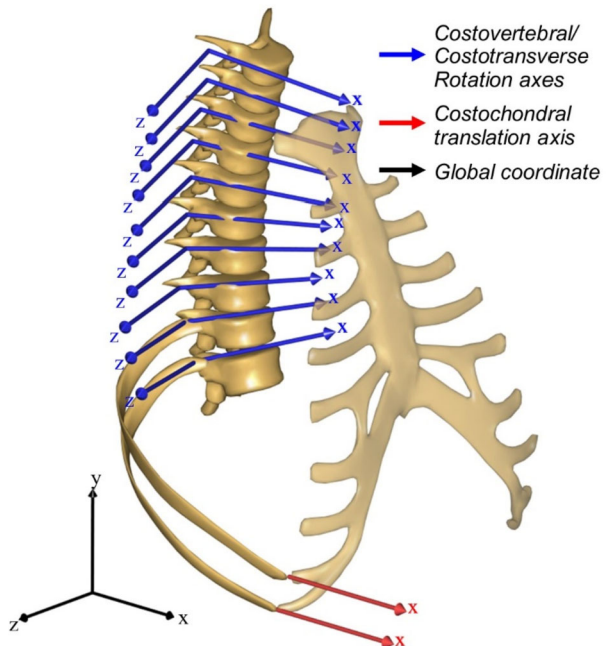


Fig. 2 (a) Transformation of the global coordinate (gray) to create the costovertebral/costotransverse coordinate system (CVCTJ coordinate in blue). (b) Schematic representation of the CVCTJ modeled as universal joints, allowing rib rotation about X_{CVCT} and Z_{CVCT} (Color figure online)

Fig. 3 All rotation axes of the right CVCTJs (blue), which follows the kyphosis angles, and ninth and tenth right CCJ translation axes (red) (Color figure online)



2.1.2 Model input: additional constraint to determine the kinematics

The whole model has 288DOFs. The joints constrain 219DOFs, which leaves 69DOFs (26DOFs are devoted to the thorax and 43DOFs are devoted to lumbar and cervical parts)

as free variables requiring 69 additional constraints to specify the model posture. In order to control the kinematics of the model reasonably, the user should estimate a set of 15 parameters from bi-planar radiographs of the patients. Figure 4 presents a schematic of the kinematic inputs in a randomly curved spine model. The sagittal view shows four inputs that can be measured from the sagittal radiograph and also the axial rotation of the apical vertebra, which can be measured from anteroposterior (AP) radiographs. The frontal view represents seven inputs that can be measured from an AP radiograph. The frontal view of the sternum and the spine illustrates the only three inputs that are relative to the sternum and they can also be measured from AP radiographs.

To create this set of drivers, careful study of spinal postures from multiple radiographs led to the following approach: the user identifies six key-vertebrae (Fig. 4), i.e. the apical vertebra of the thoracolumbar/lumbar (V_{Apex-1}) and main thorax (V_{Apex-2}) curves, and also the inferior and superior vertebrae of the lateral curves ($V_{Inferior-1}$, $V_{Superior-1}$, $V_{Inferior-2}$, $V_{Superior-2}$).

The spine was divided into four regions, which are illustrated in Fig. 4: thoracolumbar/lumbar (TL/L), main thoracic (MT), proximal thoracic (PT), and cervical. The required constraints of the spine were defined using so-called spinal rhythms, where the input is the curve angle. To control the 3D rotation of the cervical spine, a rhythm was defined, which distributes the rotation between the relevant vertebrae. In this paper, we constrained the cervical spine to hold the head vertically, which eliminates the use of input to the cervical rhythm, but this is not a necessary condition for the use of the model and the cervical spine rhythm can be easily driven by the user using an extra input for the cervical spine rhythm.

To control the lateral curvature of the spine, three rhythms were defined, respectively, on the TL/L curve between $V_{Inferior-1}$ to $V_{Superior-1}$, on the MT curve between $V_{Inferior-2}$ to $V_{Superior-2}$, and on the PT curve between $V_{Superior-2}$ to T1. In these rhythms, all the lateral rotational DOFs were constrained. The lateral rhythms use a function to distribute the curve angle to the vertebral joints in between the inferior and superior vertebrae. The angle of the inferior vertebral joint of the curve is fixed to 8% of the curve angle. The function is symmetric about the apical vertebra and tapers linearly on both sides, which means that the apical vertebra has the greatest contribution, and the sum of vertebral joint angles amounts to the specified total angle. To reconstruct lumbar lordosis and thoracic kyphosis of the spine in the sagittal plane, two rhythms were defined, spanning L5 to L1 and T12 to T1, respectively. In these rhythms, the curve angle was uniformly distributed between all vertebral joints of the curve. In the lumbar lordotic curve, all the frontal rotation DOFs were constrained. However, in the thoracic kyphosis rhythm, only five frontal rotation DOFs were constrained, i.e. T12 to T9 and T4. One spinal rhythm was defined to create axial rotation, which constrains the axial rotation DOFs between $V_{Inferior-2}$ to T8. In the following, the inputs of the model, which is a set of 15 parameters, are presented.

A review of the literature on scoliosis characteristics [45, 46, 49–53] has revealed several clinically accepted measures for scoliosis deformities and severity. Among these, the following parameters, defined by measures to anatomical landmarks, were selected as input to the model and for validation purposes. Seven of the inputs are angles between two elements (Fig. 4):

- *PLR*: defined as pelvis lateral rotation relative to the ground in the upright standing posture.
- *TL/L Cobb*: defined as the Cobb angle of the TL/L curve spanning $V_{Inferior-1}$ to $V_{Superior-1}$. In the coronal plane, the Cobb angle is defined as the greatest angle at a particular region of the spine measured from the inferior endplate of a lower vertebra to the superior endplate of an upper vertebra and considered the main factor to represent scoliotic spines.
- *MT Cobb*: defined as Cobb angle of MT curve spanning $V_{Inferior-2}$ to $V_{Superior-2}$.

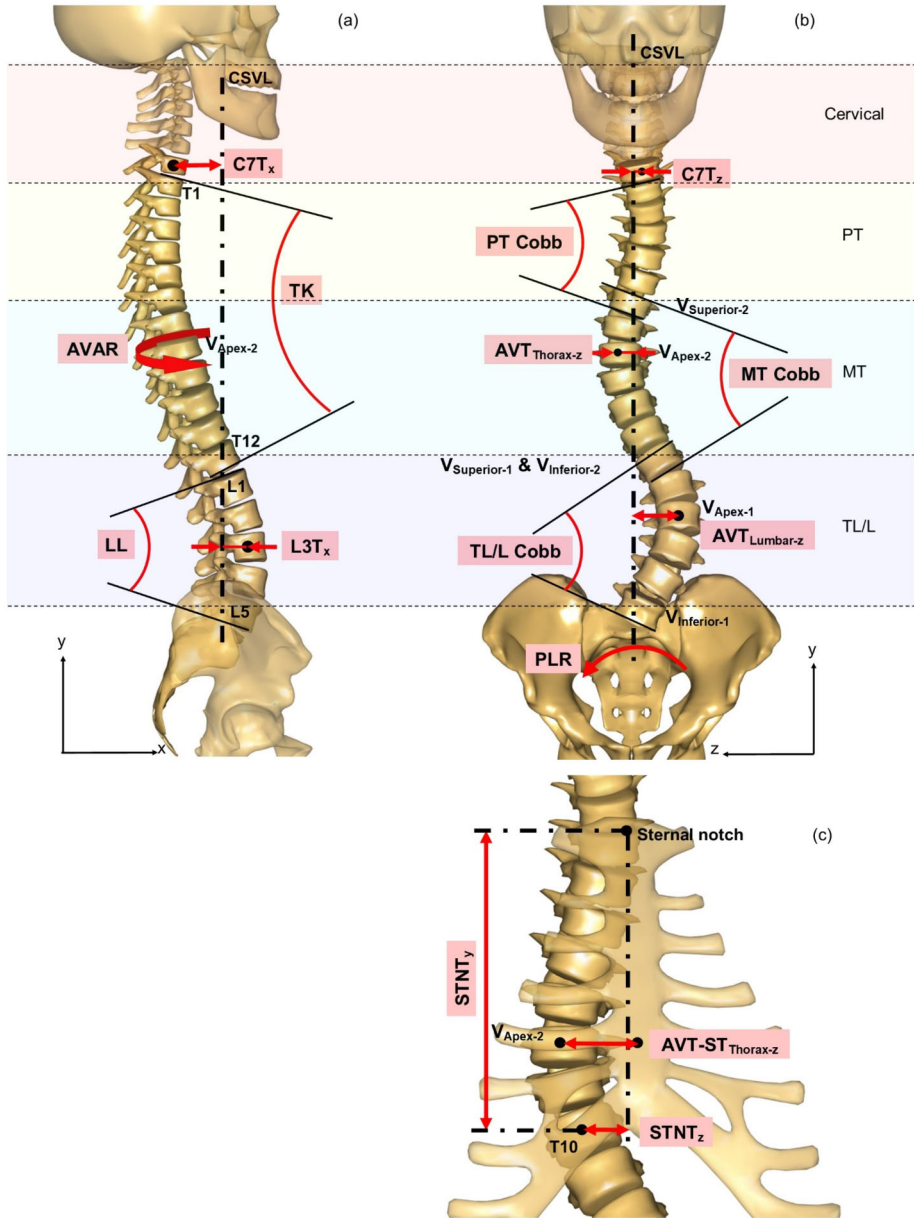


Fig. 4 Kinematic inputs in a randomly curved spine model. All inputs are illustrated with red shape fill and arrows. Six key-vertebrae are also shown in the figure. Spine regions are also represented with different background colors. (a) The sagittal view of the spine shows four inputs that can be measured from a sagittal radiograph and also the axial rotation of the apical vertebra, which can be estimated from AP radiographs. (b) The frontal view of a curved spine represents seven inputs that can be measured from the AP radiograph, (c) the frontal view of the sternum and the spine illustrates the three inputs that are relative to the sternum, and they can also be measured from AP radiograph (Color figure online)

Table 1 The set of 15 general kinematic inputs, segments that the measurements were performed relative to them, the relevant axes that the variables translate along or rotate about them

Input's No.	General kinematic inputs	Relevant segments	Axis
1	Pelvis lateral rotation (<i>PLR</i>)	Pelvis - Ground	X
2	Thoracolumbar/lumbar Cobb angle (<i>TL/L Cobb</i>)	$V_{Inferior-1} - V_{Superior-1}$	X
3	Main thoracic Cobb angle (<i>MT Cobb</i>)	$V_{Inferior-2} - V_{Superior-2}$	X
4	Proximal thoracic Cobb angle (<i>PT Cobb</i>)	$V_{Superior-2} - T1$	X
5	Lumbar lordosis angle (<i>LL</i>)	L5 - L1	Z
6	Thoracic kyphosis angle (<i>TK</i>)	T12 - T1	Z
7	V_{Apex-2} axial rotation (<i>AVAR</i>)	V_{Apex-2} - Pelvis	Y
8	V_{Apex-1} translation ($AVT_{Lumbar-z}$)	V_{Apex-1} - Pelvis	Z
9	V_{Apex-2} translation ($AVT_{Thorax-z}$)	V_{Apex-2} - Pelvis	Z
10	L3 translation ($L3T_x$)	L3 - Pelvis	X
11	C7 translation along X ($C7T_x$)	C7 - Sacrum	X
12	C7 translation along Z ($C7T_z$)	C7 - Sacrum	Z
13	V_{Apex-2} translation ($AVT-ST_{Thorax-z}$)	V_{Apex-2} - Sternum	Z
14	Sternal notch translation along Y ($STNT_y$)	Sternum - T10	Y
15	Sternal notch translation along Z ($STNT_z$)	Sternum - T10	Z

- *PT Cobb*: defined as Cobb angle of PT curve spanning $V_{Superior-2}$ to T1.
- *LL*: lumbar lordosis is defined as an angle from the inferior endplate of L5 to the superior endplate of L1.
- *TK*: thoracic kyphosis is an angle from inferior endplate T12 to superior endplate T1.
- *AVAR*: defined as the axial rotation of the apical vertebra (V_{Apex-2}) relative to the pelvis.

The other eight inputs are distances between two segments' nodes (Fig. 4) and some of them are measured relative to the central sacrum vertical line on the frontal and sagittal view (CSVL), which is a vertical line from the posterior superior endplate of the sacrum.

- $AVT_{Lumbar-z}$: defined as the translation of the lumbar apex (V_{Apex-1}) along the z-axis relative to the pelvis, which was measured relative to CSVL.
- $AVT_{Thorax-z}$: defined as the translation of the thorax apex (V_{Apex-2}) along the z-axis relative to the pelvis, which was measured relative to CSVL.
- $L3T_x$: defined as L3 translation along x-axis relative to the pelvis, which was measured relative to CSVL.
- $C7T_x$, $C7T_z$: defined as C7 translation along x and z axes relative to the sacrum, respectively, which were measured relative to CSVL. These parameters describe the coronal and sagittal balance [54].
- $AVT-ST_{Thorax-z}$: defined as the translation of the thorax apex (V_{Apex-2}) along z-axis relative to a sternum node that is in the apical transverse plane.
- $STNT_y$, $STNT_z$: defined as the lateral and longitudinal translation of the sternal notch (along y and z axes) relative to T10, respectively.

Table 1 represents the set of 15 general kinematic inputs, segments defining the measurements, and the axes that the segments translate along or rotate about.

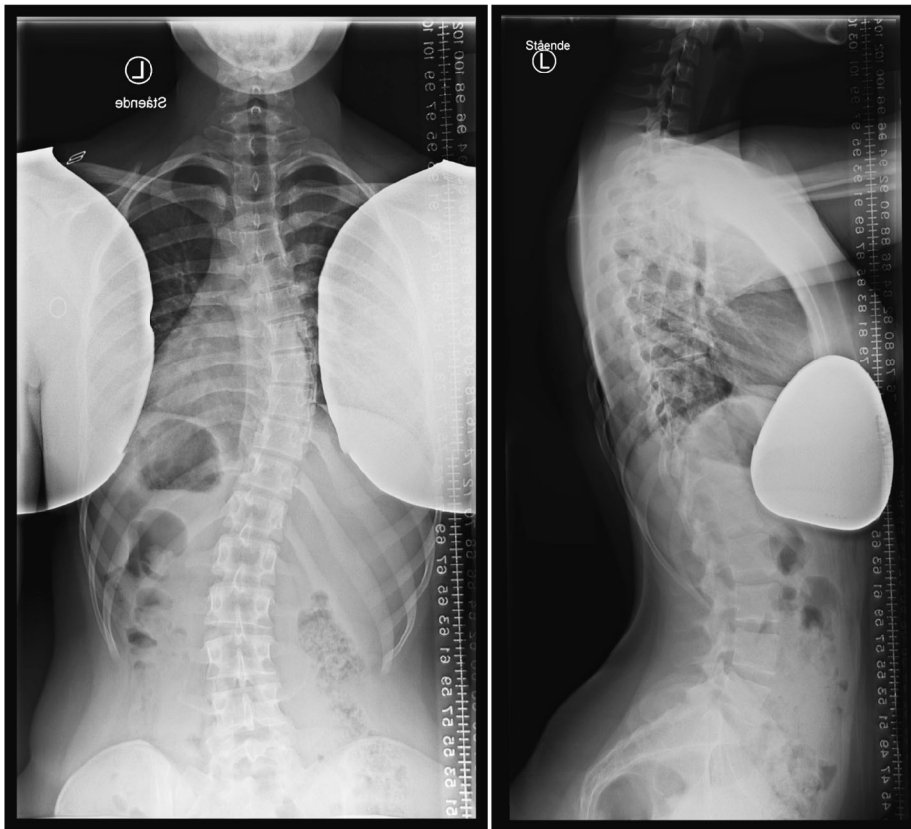


Fig. 5 The AP and sagittal radiographs of the patient. The left picture was flipped, so the left side of the picture is the left side of the patient. The patient was 17-year-old with a right MT curve with a 33° Cobb angle and a minor left TL/L curve with a 24° Cobb angle

2.2 Radiographic imaging

Two-dimensional radiography is already performed in the clinical routine of AIS patients but CT scanning is avoided in the interest of radiation dose minimization for adolescents. Bi-planar radiography is a considerable clinical advantage compared to single-plane X-rays [55]. The required inputs described in the preceding section were measured from AP and lateral radiographs of the whole spine and the ribcage in the relaxed standing position. The radiographic measurement was carried out by an experienced pediatric surgeon treating scoliosis using the Synedra view software.

2.2.1 Participant

A 17-year-old scoliosis patient with a right MT curve of 33° Cobb angle and a minor left TL/L curve with a 24° Cobb angle was used as a sample. The AP and sagittal radiographs of the patient are represented in Fig. 5. This study was evaluated and approved by the local Research Ethics Committee (Journal number: H17034237). We obtained oral and written consent from the patient, and the study was conducted according to national guidelines and the Helsinki Declaration.

Table 2 Key-vertebrae recognized from bi-planar radiographs

Key-vertebrae	Recognized from radiographs
V_{Apex-1}	L3
V_{Apex-2}	T8
$V_{Inferior-1}$	L5
$V_{Superior-1}$	T11
$V_{Inferior-2}$	T10
$V_{Superior-2}$	T6

2.3 Scaling the model

The baseline dimensions of the bony elements are based on the reconstruction of the male anatomy of a body with 62 cm trunk height, available in the AnyBody Managed Model Repository (AMMR 2.3). The participant's spine length, ribcage width and ribcage depth were measured from the radiographs. The spine length from the superior endplate of the sacrum to C7 is 46 cm based on the AP radiographs, which results in a longitudinal scale factor of 0.74 by which the vertebral column, including the pelvis and skull in the standing and normal spine posture, were scaled uniformly. The ribcage was scaled with a separate factor for each axis direction to more precisely represent the participant. Measuring the ribcage width from the AP radiograph results in a mediolateral scale factor of 0.79. The ribcage depth was measured from the center of T8 to the sternum in the sagittal radiograph, from which an anteroposterior scale factor of 0.83 was calculated.

2.4 Simulation

Quasi-static simulation of the 3D motion of the whole spine and ribcage was performed. The simulation started with a healthy spine and finished with a scoliotic spine, which corresponds to the patient in the upright standing posture.

3 Results

3.1 Create the patient-specific model

3.1.1 Identifying the key-vertebrae from radiographs

The key-vertebrae were identified from the radiographs and are listed in Table 2.

3.1.2 Measurement of the model's input from radiographs

The 15 input parameters were defined based on the key-vertebrae and were measured from radiographs. Angles and distances were calculated in degree and mm, respectively. Table 3 presents the set of 15 patient-specific kinematic inputs, the translation/rotation axes, and the measured values from radiographs. Most of the inputs were easily measurable from the radiographs (Fig. 5). The axial rotation of T8 was measured from the AP radiograph using a method by Chi et al. [56]. The sternal notch was estimated as the middle point of the line passing through the clavicles, and the sternum position was estimated using a perpendicular line to that line from the sternal notch.

Table 3 The set of 15 kinematic inputs, the relevant axes, and the measured values from radiographs

Number	Kinematic variable	Axis	Measured value
1	<i>PLR</i>	X	0°
2	<i>TL/L Cobb angle</i>	X	24°
3	<i>MT Cobb angle</i>	X	33°
4	<i>PT Cobb angle</i>	X	8°
5	<i>LL</i>	Z	44°
6	<i>TK</i>	Z	23°
7	<i>AVAR</i>	Y	14°
8	<i>AVT_{Lumbar-z}</i>	Z	7 mm
9	<i>AVT_{Thorax-z}</i>	Z	24 mm
10	<i>L3T_x</i>	X	30 mm
11	<i>C7T_x</i>	X	40 mm
12	<i>C7T_z</i>	Z	2 mm
13	<i>AVT-ST_{Thorax-z}</i>	Z	23 mm
14	<i>STNT_y</i>	Y	165 mm
15	<i>STNT_z</i>	Z	15 mm

3.2 Validation from radiographs

Dependent kinematic variables with clinical relevance were selected for validation purposes and compared with measurements from radiographs, defining the difference between dependent parameters and measurements as an error. These validation parameters are:

- RH_{10} , RH_8 , RH_5 : Rib hump is the linear distance between the left and right posterior rib prominences along the x-axis defining RH_i at the i th thoracic level of the rib deformity; it represents the truncal rotation and concavity and convexity of the patient's back. Figure 6 displays the sagittal and top views of the scoliosis skeletal model representing the rib hump of the fifth, eighth, and tenth levels.
- RVA_{R_i} , RVA_{L_i} and $RVAD_i$ of the tenth to sixth level, and $RVAD_4$: The rib-vertebra angle difference ($RVAD_i$) of the i th thoracic level is defined as the difference between the rib-vertebra angle (RVA) of the concave (left side in this case, which is called RVA_{L_i}) and convex (in this case RVA_{R_i}) sides of the curved spine; the RVA is defined as the angle between a line joining the center of the rib head and rib neck, and a second line perpendicular to the inferior endplate of the vertebra. Figure 6 illustrates the posterior view of the model representing the measurement and calculation of the RVA_{R_8} , RVA_{L_8} , and $RVAD_8$.
- $STFA$: Sternum frontal angle is the manubrium angle about the z-axis relative to the vertical line, which is visible from the lateral radiograph.
- RSD : Rib spread difference is the difference of the left and right intercostal distances at twelfth and seventh rib levels along the y-axis measured at the lateral transverse process (Fig. 6).
- AVB_R : The apical vertebral body-rib ratio is the ratio of linear measurements from the lateral borders of the apical thoracic vertebrae to the chest wall.
- HI : Haller index is the ratio of sagittal diameter (from apical vertebra to the sternum) to the frontal diameter of the ribcage.
- The TK was used in a rhythm for driving L1 to T9 plus T4 joints but the rhythm did not drive T9 to T1 vertebral joints except T4. In other words, the model does not use TK to

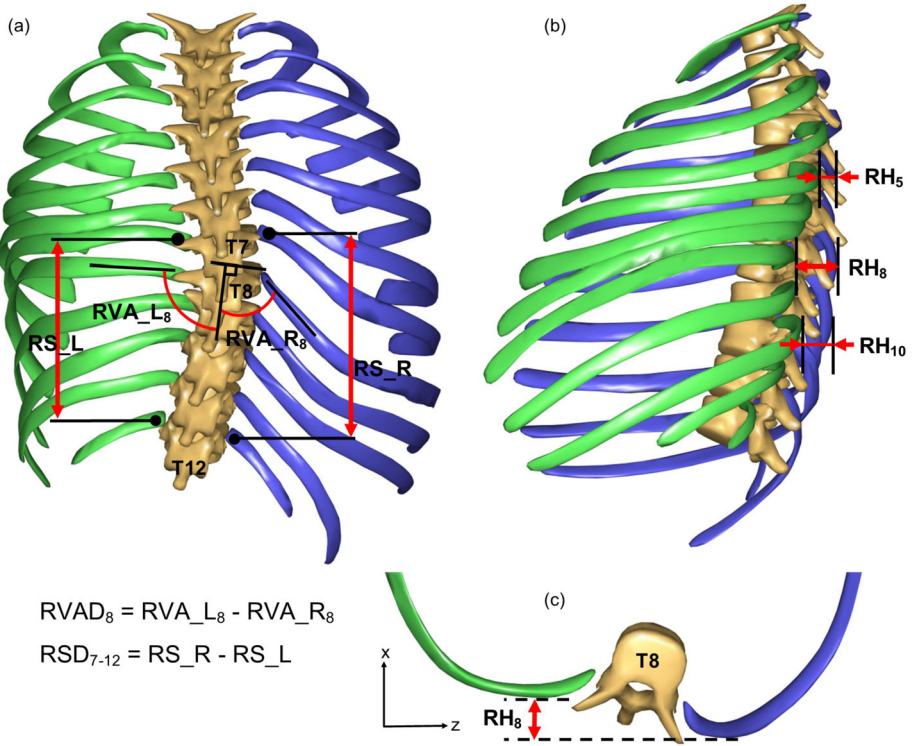


Fig. 6 Left and right ribs are illustrated in green and blue colors, respectively. (a) The posterior view of the model represents rib-vertebra angles in the right (RVA_{R_8}) and left (RVA_{L_8}) sides in the apical level (eighth level) and the $RVAD_8$ measurement. It also illustrates the rib spread from seventh to twelfth level in the right (RS_R) and left (RS_L) sides and calculation of the relevant RSD. (b) The RH_5 , RH_8 , RH_{10} in the fifth, eighth, and tenth levels have been shown using the sagittal view of the model. (c) top view illustration of RH_8 (Color figure online)

control the thoracic kyphosis angle of the whole but a part of the spine. Thus, TK can also be used as a parameter for validation.

The mentioned kinematic variables, the relevant axes, measurements from radiographs, measurements from model projection into 2D, and their errors are listed in Table 4. The average errors of RVAs and RVADs, which were calculated around the apex, were 6.6° and 9.0° . The average errors of rib hump were 6.3 mm.

Figure 7 shows the posterior, anterior, and left view of the resultant scoliosis skeletal model in the upright standing posture. For visual assessment, the simulated spine was projected to the radiographs in both sagittal and frontal views (Fig. 8).

4 Discussion

Understanding the aetiopathogenesis of scoliosis and developing new prevention methods, exercises, and rehabilitation procedures requires a comprehensive kinematic analysis of the spine and ribcage, as well as joint and muscle loading patterns in the trunk. Biomechanically valid musculoskeletal models of the thoracic region predispose a correct definition of the

Table 4 The kinematic variables for validation purposes, the relevant axes, measurements from radiographs, measurements from model projection into 2D, and their absolute errors

	Kinematic variable	Axis	Measured from radiographs	Measured from model	Error
1	RH_{10}	X	39 mm	25 mm	14 mm
2	RH_8 (Apex)	X	33 mm	30 mm	3 mm
3	RH_5	X	14 mm	12 mm	2 mm
4	RVA_{R10}	X	41°	48°	7°
5	RVA_{L10}	X	52°	67°	15°
6	RVA_{R9}	X	47°	55°	8°
7	RVA_{L9}	X	73°	71°	2°
8	RVA_{R8} (Apex)	X	46°	42°	4°
9	RVA_{L8} (Apex)	X	81°	93°	12°
10	RVA_{R7}	X	50°	47°	3°
11	RVA_{L7}	X	92°	98°	6°
12	RVA_{R6}	X	46°	48°	2°
13	RVA_{L6}	X	101°	94°	7°
14	$RVAD_{10}$	X	11°	18°	7°
15	$RVAD_9$	X	26°	16°	10°
16	$RVAD_8$ (Apex)	X	35°	51°	16°
17	$RVAD_7$	X	42°	51°	9°
18	$RVAD_6$	X	55°	46°	9°
19	$RVAD_4$	X	23°	20°	3°
20	$STFA$	Z	37°	37°	0°
21	RSD	Y	20 mm	14 mm	6 mm
22	AVB_R	-	0.64	0.86	0.22
23	HI	-	0.43	0.5	0.07
24	TK	Z	23°	30°	7°

ribcage kinematics. The ribcage contains multiple closed loops connecting the ribs to the sternum, resulting in a complex model. The main contribution of the present work was to work out a kinematically determinate and anatomically compatible constraint strategy for this model.

The constraint definitions should represent the anatomical joint properties while allowing the model to attain different types of scoliotic postures known from clinical practice. This goal was reached by defining a set of 15 clinically relevant kinematic constraints, most of which are already employed to assess the severity of the scoliotic spine [45, 46, 49–53].

Costovertebral and costotransverse joints were previously modeled as compound revolute and spherical joint. We redefined these as universal joints based on reported anatomical studies. Articulations between ribs and the sternum were defined as spherical joints except in the ninth and tenth levels, which have one additional anteroposterior DOF. With this joint definition, the model can simulate different kinds of lateral bending using three Cobb angles. Most scoliosis patients have rib prominence, especially when they bend forward. Due to the restriction of longitudinal rib rotation, the model mimics this behavior and reproduces a similar pattern of rib hump. Moreover, the model can simulate rib rotations about the

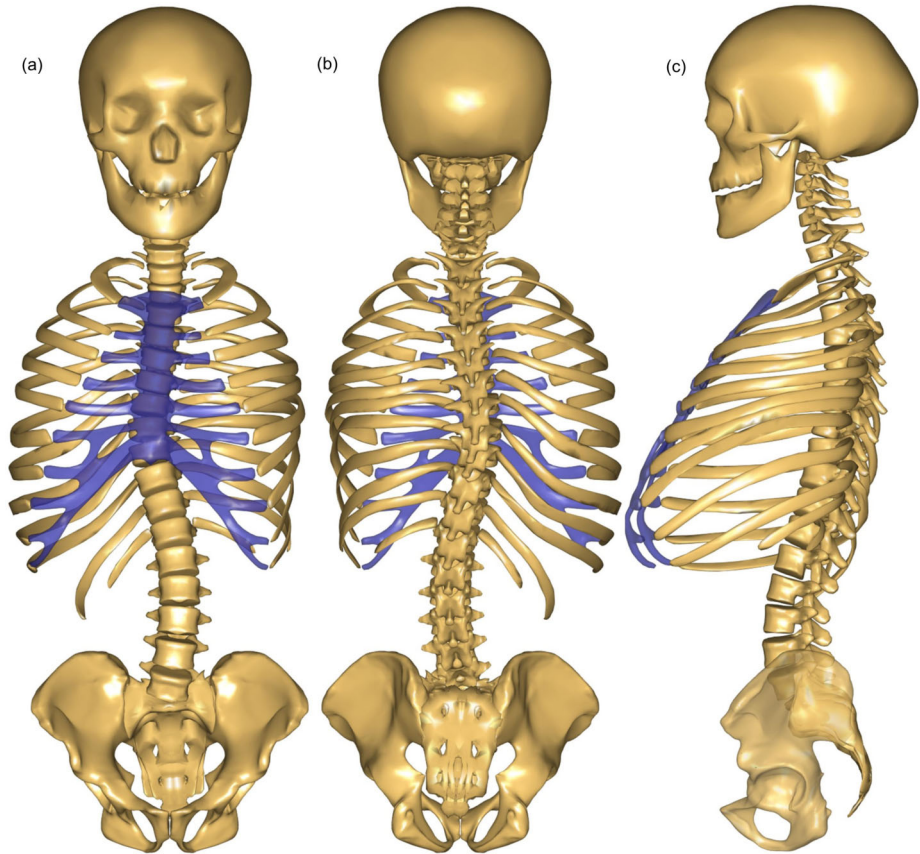


Fig. 7 (a) Anterior, (b) posterior, and (c) left view of the scoliosis skeletal model in the upright standing posture. The sternum is shown in transparent blue color (Color figure online)

frontal axis to model specific tasks such as inhaling, exhaling, flexion, and rotation about the anteroposterior axis to model the different kinds of deformities.

One of the observable effects of scoliosis upon the thoracic cage is an increased downward tilt of the ribs on the convex as compared with the concave side, maximal at the apex of the curve [57], which can be quantified by RVAD. The rib asymmetry is an adaptive response of the ribs, secondary to vertebral rotation as a contrary effect to primary involvement in the pathomechanism of the deformation [58]. The average error of RVADs was 9° , and the greatest error of RVAD was placed at the apex level, which was 16° . The average error of RVAs was 6.6° , and the greatest errors of RVAs occurred in the $RVA_{L_{10}}$, and RVA_{L_8} , which were 15° , and 12° , respectively. Since we only had one patient in this study, to make the comparison more understandable, T6 to T10 and their relative ribs of the model were projected to the radiograph in the posterior view for visual comparison in Fig. 9 (a), which implies that the model followed the patient's rib angle trend in both right and left sides with reasonable errors. Please notice that the model is kinematically determinate and provides RVADs as dependent output variables.

The coupled motion of lateral and axial rotation of the vertebrae leads ribs to rotate, thus facilitating the rib hump [59]. Rib prominences of the lower ribs are greater in this patient,

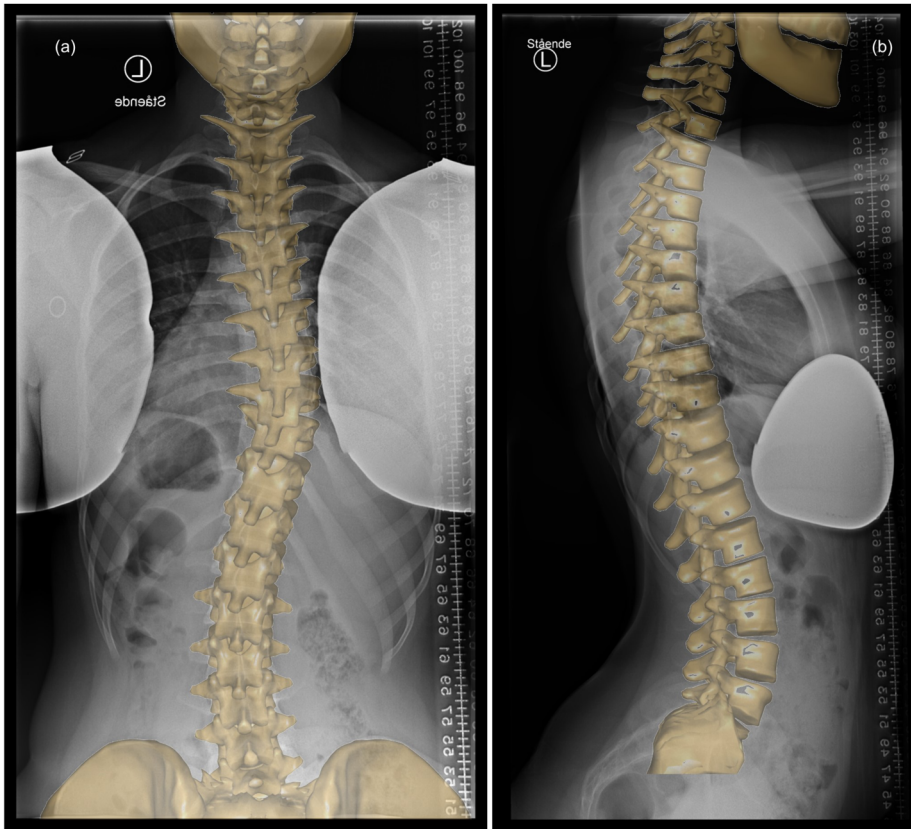


Fig. 8 The simulated spine (light yellow color) was projected to the radiographs in both frontal (a) and sagittal (b) views for validation purposes (Color figure online)

according to the lateral radiograph. The model also generated the same pattern for the rib prominence, therefore again supporting the constraint definitions. The errors of the model for RH_{10} , RH_8 , and RH_5 were 14, 3, and 2 mm, respectively, and the average error of RHs was 6.3 mm. Ribs in the eighth and tenth levels were projected to the radiograph in the sagittal view in Fig. 9 (b). The measurement of RH_8 and RH_{10} are shown using yellow and white colors in the model projection and the radiograph, respectively. Even though the error of the RH_8 is small, both the right and the left ribs of the patient are placed further posteriorly than the model's ribs. However, Fig. 9 (b) shows that the model followed the rib prominence trend of the radiograph.

Besides, on the convex side, ribs are more separated at their margins compared to the concave side [59], which can be quantified by defining RSD . The error of the RSD is 6 mm. One of the assessment parameters for the overall thoracic and rib deformity is $AVB-R$ [51], which describes the translation of the apical vertebra relative to the rib's sides. The errors of the $AVB-R$ and HI are directly relative to the scaling, and in this case, they are 0.22 and 0.07, respectively. The TK and $STFA$ were generated with errors of 7° and 0° . The model generated the RSD and $AVB-R$, TK , and $STFA$ with reasonable errors.

The model appeared to visually reproduce the rib deformation pattern conforming to radiographs, results in simulating the rib prominence, rib spread, and rib-vertebra angles. The

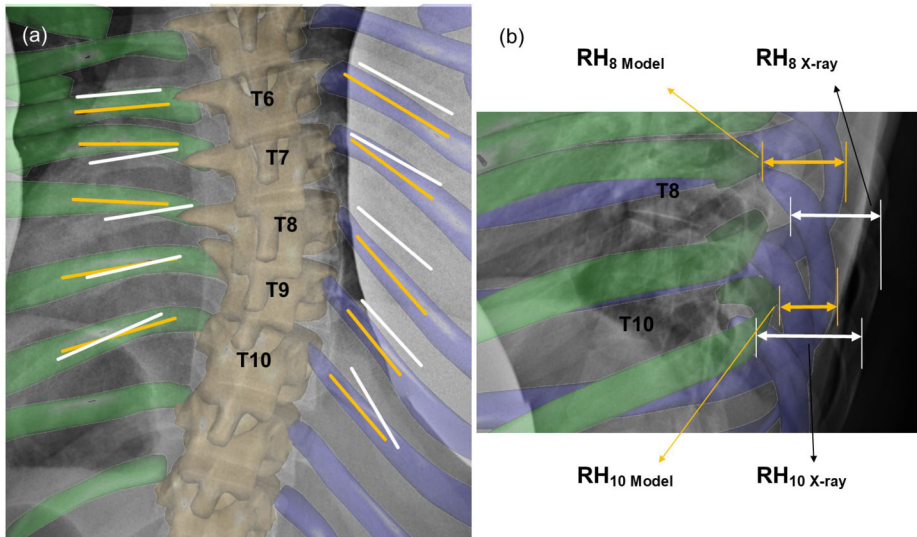


Fig. 9 Left and right ribs are illustrated in green and blue colors, respectively. (a) T6 to T10 and their relative ribs of the model were projected to the radiograph in the posterior view for visual comparison. The yellow and white lines present the head-to-neck lines of the ribs in the model projection and the radiograph, respectively. (b) Ribs in the eighth and tenth levels were projected to the radiograph in the sagittal view, and the measurement of RH_8 and RH_{10} are shown using yellow and white colors in the model projection and the radiograph, respectively (Color figure online)

measured errors were acceptable with the notable difference of RH_{10} and $RVAD_8$. Please notice that, since the initial fitting of the model to the patient was done with a scaling rather than a 3D reconstruction to actual bone shapes, the observed errors between dependent and measured validation variables comprise scaling errors as well as kinematic errors.

In this paper, we represented a base model that can simulate subject-specific curved spines, albeit with subject-specific bone shapes created by a relatively crude non-uniform scaling. Considering that AIS can lead to bone deformity, patient-specific 3D reconstruction of bone shapes is an obvious improvement for future work. Another limitation of this work is measurement of the variables from radiographs. Some of the variables, such as vertebral rotation or sternum position, are not directly measurable and need estimation, which can be a source of error in low-quality radiographs. However, ordinary radiographs are considered the golden standard of current clinical scoliosis evaluation, whereas new 2D/3D recording methods, such as the EOS system, which can estimate these parameters more precisely, is unavailable in most clinical settings. In near-future clinical use of the model, the recommendation is to select the set of independent drivers according to which parameters can be measured reliably in low-quality radiographs. Please notice that the Cartesian method underlying the simulation makes no assumption on constraint sequence, thus allows for the exchange of constraints without further model modifications.

5 Conclusions

A detailed study of clinical data describing ribcage deformation led to the definition of a set of kinematically determinate, holonomic constraints in the human thoracolumbar system

and the implementation of these into the complete model of the human thorax. The resulting model is controlled by a set of 15 drivers relating to clinical metrics of scoliosis. The model qualitatively reproduces the spine and ribcage deformation pattern and reproduces the most dependent metrics with acceptable errors. Correct kinematic constraints are a condition for the subsequent use of the model to investigate the kinetics of scoliosis pathomechanism. Forthcoming work will attempt kinetic verification of the loading patterns. If the model can subsequently be shown to reproduce the kinetics of scoliosis, then it can also be used for in-silico design of interventions such as advanced orthotics to manage the condition.

Acknowledgements This project has received funding from the European Union's Horizon 2020 research and innovation programme under the Marie Skłodowska-Curie grant agreement No. [764644].

Funding This project has received funding from the European Union's Horizon 2020 research and innovation programme under the Marie Skłodowska-Curie grant agreement No. [764644].

Data availability After an internal review, the model will be made publicly available through <https://doi.org/10.5281/zenodo.3932764>.

Code availability The software to run the model is The AnyBody Modeling System, available from AnyBody Technology A/S, www.anybodytech.com.

Conflicts of interest/Competing interests John Rasmussen owns stock and is a board member of AnyBody Technology A/S, whose software is used for model development.

Pavel Galibarov is employed in AnyBody Technology A/S.

Ethics approval, Consent to participate, Consent for publication This study was evaluated and approved by the local Research Ethics Committee (Journal number: H17034237). We obtained oral and written consent from the patient, and the study was conducted according to national guidelines and the Helsinki Declaration.

Publisher's Note Springer Nature remains neutral with regard to jurisdictional claims in published maps and institutional affiliations.

References

1. Wong, C.: Mechanism of right thoracic adolescent idiopathic scoliosis at risk for progression; a unifying pathway of development by normal growth and imbalance. *Scoliosis* **10**, 1–5 (2015). <https://doi.org/10.1186/s13013-015-0030-2>
2. Machida, M., Weinstein, S.L., Dubousset, J.: *Pathogenesis of Idiopathic Scoliosis*. Springer, Tokyo (2018)
3. Cheng, J.C., Castelein, R.M., Chu, W.C., Danielsson, A.J., Dobbs, M.B., Grivas, T.B., Gurnett, C.A., Luk, K.D., Moreau, A., Newton, P.O., Stokes, I.A., Weinstein, S.L., Burwell, R.G.: Adolescent idiopathic scoliosis. *Nat. Rev. Dis. Primers* **1**, 15030 (2015). <https://doi.org/10.1038/nrdp.2015.30>
4. Scoliosis Research Society (SRS): (2021). <https://www.srs.org/>. Accessed 24 February 2021
5. Jalalian, A., Gibson, I., Tay, E.H.: Computational biomechanical modeling of scoliotic spine: challenges and opportunities. *Spine Deform.* **1**, 401–411 (2013). <https://doi.org/10.1016/j.jspd.2013.07.009>
6. Villemure, I., Aubin, C.E., Dansereau, J., Labelle, H.: Biomechanical simulations of the spine deformation process in adolescent idiopathic scoliosis from different pathogenesis hypotheses. *Eur. Spine J.* **13**, 83–90 (2004). <https://doi.org/10.1007/s00586-003-0565-4>
7. Driscoll, M., Mac-Thiong, J.M., Labelle, H., Parent, S.: Development of a detailed volumetric finite element model of the spine to simulate surgical correction of spinal deformities. *BioMed Res. Int.* **2013**, 931741 (2013). <https://doi.org/10.1155/2013/931741>
8. Cahill, P.J., Wang, W., Asghar, J., Booker, R., Betz, R.R., Ramsey, C., Baran, G.: The use of a transition rod may prevent proximal junctional kyphosis in the thoracic spine after scoliosis surgery: a finite element analysis. *Spine* **37**, 687–695 (2012). <https://doi.org/10.1097/BRS.0b013e318246d4f2> (Phila. Pa. 1976)

9. Monteiro, N.M.B., da Silva, M.P.T., Folgado, J.O.M.G., Melancia, J.P.L.: Structural analysis of the intervertebral discs adjacent to an interbody fusion using multibody dynamics and finite element cosimulation. *Multibody Syst. Dyn.* **25**, 245–270 (2011). <https://doi.org/10.1007/s11044-010-9226-7>
10. Stokes, I.A.F., Laible, J.P.: Three-dimensional osseo-ligamentous model of the thorax representing initiation of scoliosis by asymmetric growth. *J. Biomech.* **23**, 589–595 (1990). [https://doi.org/10.1016/0021-9290\(90\)90051-4](https://doi.org/10.1016/0021-9290(90)90051-4)
11. Duke, K., Aubin, C.-E., Dansereau, J., Labelle, H.: Biomechanical simulations of scoliotic spine correction due to prone position and anaesthesia prior to surgical instrumentation. *Clin. Biomech.* **20**, 923–931 (2005). <https://doi.org/10.1016/J.CLINBIOMECH.2005.05.006>
12. Sevrain, A., Aubin, C.E., Gharbi, H., Wang, X., Labelle, H.: Biomechanical evaluation of predictive parameters of progression in adolescent isthmic spondylolisthesis: a computer modeling and simulation study. *Scoliosis* **7**, 1–9 (2012). <https://doi.org/10.1186/1748-7161-7-2>
13. Solomonow, M., Zhou, B.-H., Harris, M., Lu, Y., Baratta, R.V.: The ligamento-muscular stabilizing system of the spine. *Spine* **23**, 2552–2562 (1998). <https://doi.org/10.1097/00007632-199812010-00010> (Phila. Pa. 1976)
14. du Rose, A., Breen, A.: Relationships between paraspinal muscle activity and lumbar inter-vertebral range of motion. *Healthcare* **4**, 4 (2016). <https://doi.org/10.3390/healthcare4010004>
15. Rohlmann, A., Bauer, L., Zander, T., Bergmann, G., Wilke, H.J.: Determination of trunk muscle forces for flexion and extension by using a validated finite element model of the lumbar spine and measured in vivo data. *J. Biomech.* **39**, 981–989 (2006). <https://doi.org/10.1016/j.jbiomech.2005.02.019>
16. Wang, W., Baran, G.R., Betz, R.R., Samdani, A.F., Pahys, J.M., Cahill, P.J.: The use of finite element models to assist understanding and treatment for scoliosis: a review paper. *Spine Deform.* **2**, 10–27 (2014). <https://doi.org/10.1016/j.jspd.2013.09.007>
17. Ezquerro, F., Simón, A., Prado, M., Pérez, A.: Combination of finite element modeling and optimization for the study of lumbar spine biomechanics considering the 3D thorax-pelvis orientation. *Med. Eng. Phys.* **26**, 11–22 (2004). [https://doi.org/10.1016/S1350-4533\(03\)00128-0](https://doi.org/10.1016/S1350-4533(03)00128-0)
18. Huynh, A.M., Aubin, C.E., Mathieu, P.A., Labelle, H.: Simulation of progressive spinal deformities in Duchenne muscular dystrophy using a biomechanical model integrating muscles and vertebral growth modulation. *Clin. Biomech.* **22**, 392–399 (2007). <https://doi.org/10.1016/j.clinbiomech.2006.11.010>
19. Kamal, Z., Rouhi, G., Arjmand, N., Adeeb, S.: A stability-based model of a growing spine with adolescent idiopathic scoliosis: a combination of musculoskeletal and finite element approaches. *Med. Eng. Phys.* **64**, 46–55 (2019). <https://doi.org/10.1016/j.medengphy.2018.12.015>
20. Shirazi-Adl, A., El-Rich, M., Pop, D.G., Parnianpour, M.: Spinal muscle forces, internal loads and stability in standing under various postures and loads—application of kinematics-based algorithm. *Eur. Spine J.* **14**, 381–392 (2005). <https://doi.org/10.1007/s00586-004-0779-0>
21. Abouhossein, A., Weisse, B., Ferguson, S.J.: A multibody modelling approach to determine load sharing between passive elements of the lumbar spine. *Comput. Methods Biomech. Biomed. Eng.* **14**, 527–537 (2011). <https://doi.org/10.1080/10255842.2010.485568>
22. Stokes, I.A.F., Gardner-Morse, M.: Lumbar spine maximum efforts and muscle recruitment patterns predicted by a model with multijoint muscles and joints with stiffness. *J. Biomech.* **28**, 173–186 (1995). [https://doi.org/10.1016/0021-9290\(94\)E0040-A](https://doi.org/10.1016/0021-9290(94)E0040-A)
23. Galbusera, F., Wilke, H.-J., Brayda-Bruno, M., Costa, F., Fornari, M.: Influence of sagittal balance on spinal lumbar loads: a numerical approach. *Clin. Biomech.* **28**, 370–377 (2013). <https://doi.org/10.1016/J.CLINBIOMECH.2013.02.006>
24. Raabe, M.E., Chaudhari, A.M.W.: An investigation of jogging biomechanics using the full-body lumbar spine model: model development and validation. *J. Biomech.* **49**, 1238–1243 (2016). <https://doi.org/10.1016/j.jbiomech.2016.02.046>
25. Christophy, M., Adila, N., Senan, F., Lotz, J.C., Reilly, O.M.O.: A musculoskeletal model for the lumbar spine. *Biomech. Model. Mechanobiol.* **11**, 19–34 (2012). <https://doi.org/10.1007/s10237-011-0290-6>
26. Arshad, R., Zander, T., Dreischarf, M., Schmidt, H.: Influence of lumbar spine rhythms and intra-abdominal pressure on spinal loads and trunk muscle forces during upper body inclination. *Med. Eng. Phys.* **38**, 333–338 (2016). <https://doi.org/10.1016/j.medengphy.2016.01.013>
27. Christophy, M., Curtin, M., Faruk Senan, N.A., Lotz, J.C., O'Reilly, O.M.: On the modeling of the intervertebral joint in multibody models for the spine. *Multibody Syst. Dyn.* **30**, 413–432 (2013). <https://doi.org/10.1007/s11044-012-9331-x>
28. de Zee, M., Hansen, L., Wong, C., Rasmussen, J., Simonsen, E.B.: A generic detailed rigid-body lumbar spine model. *J. Biomech.* **40**, 1219–1227 (2007). <https://doi.org/10.1016/j.jbiomech.2006.05.030>
29. Arjmand, N., Shirazi-Adl, A.: Model and in vivo studies on human trunk load partitioning and stability in isometric forward flexions. *J. Biomech.* **39**, 510–521 (2006). <https://doi.org/10.1016/J.JBIOMECH.2004.11.030>

30. Jalalian, A., Tay, F.E.H., Arastehfar, S., Liu, G.: A patient-specific multibody kinematic model for representation of the scoliotic spine movement in frontal plane of the human body. *Multibody Syst. Dyn.* **39**, 197–220 (2017). <https://doi.org/10.1007/s11044-016-9556-1>
31. Harrison, D.E., Colloca, C.J., Harrison, D.D., Janik, T.J., Haas, J.W., Keller, T.S.: Anterior thoracic posture increases thoracolumbar disc loading. *Eur. Spine J.* **14**, 234–242 (2005). <https://doi.org/10.1007/s00586-004-0734-0>
32. Keller, T.S., Colloca, C.J., Harrison, D.E., Harrison, D.D., Janik, T.J.: Influence of spine morphology on intervertebral disc loads and stresses in asymptomatic adults: implications for the ideal spine. *Spine J.* **5**, 297–309 (2005). <https://doi.org/10.1016/j.spinee.2004.10.050>
33. Briggs, A.M., van Dieën, J.H., Wrigley, T.V., Greig, A.M., Phillips, B., Lo, S.K., Bennell, K.L.: Thoracic kyphosis affects spinal loads and trunk muscle force. *Phys. Ther.* **87**, 595–607 (2007). <https://doi.org/10.2522/ptj.20060119>
34. Watkins, R., Watkins, R., Williams, L., Ahlbrand, S., Garcia, R., Karamanian, A., Sharp, L., Vo, C., Hedman, T.: Stability provided by the sternum and rib cage in the thoracic spine. *Spine* **30**, 1283–1286 (2005). <https://doi.org/10.1097/01.brs.0000164257.69354.bb> (Phila. Pa. 1976)
35. Brasiliense, L.B.C., Lazaro, B.C.R., Reyes, P.M., Dogan, S., Theodore, N., Crawford, N.R.: Biomechanical contribution of the rib cage to thoracic stability. *Spine* **36**, E1686–E1693 (2011). <https://doi.org/10.1097/BRS.0b013e318219ce84> (Phila. Pa. 1976)
36. Sham, M.L., Zander, T., Rohlmann, A., Bergmann, G.: Effects of the rib cage on thoracic spine flexibility/Einfluss des Brustkorbs auf die Flexibilität der Brustwirbelsäule. *Biomed. Tech. Eng.* **50**, 361–365 (2005). <https://doi.org/10.1515/BMT.2005.051>
37. Bruno, A.G., Bouxsein, M.L., Anderson, D.E.: Development and validation of a musculoskeletal model of the fully articulated thoracolumbar spine and rib cage. *J. Biomech. Eng.* **137**, 081003 (2015). <https://doi.org/10.1115/1.4030408>
38. Ignasiak, D., Dendorfer, S., Ferguson, S.J.: Thoracolumbar spine model with articulated ribcage for the prediction of dynamic spinal loading. *J. Biomech.* **49**, 959–966 (2016). <https://doi.org/10.1016/j.jbiomech.2015.10.010>
39. Bayoglu, R., Galibarov, P.E., Verdonschot, N., Koopman, B., Homminga, J.: Twente Spine Model: a thorough investigation of the spinal loads in a complete and coherent musculoskeletal model of the human spine. *Med. Eng. Phys.* **68**, 35–45 (2019). <https://doi.org/10.1016/j.medengphy.2019.03.015>
40. Higuchi, R., Komatsu, A., Iida, J., Iwami, T., Shimada, Y.: Construction and validation under dynamic conditions of a novel thoracolumbar spine model with defined muscle paths using the wrapping method. *J. Biomech. Sci. Eng.* (2019). <https://doi.org/10.1299/jbse.18-00432>
41. Damsgaard, M., Rasmussen, J., Christensen, S.T., Surma, E., de Zee, M.: Analysis of musculoskeletal systems in the AnyBody Modeling System. *Simul. Model. Pract. Theory* **14**, 1100–1111 (2006). <https://doi.org/10.1016/j.simpat.2006.09.001>
42. Nikravesh, P.E.: *Planar Multibody Dynamics: Formulation, Programming and Applications*. CRC Press, Boca Raton (2007)
43. de Zee, M., Falla, D., Farina, D., Rasmussen, J.: A detailed rigid-body cervical spine model based on inverse dynamics. *J. Biomech.* **40**, S284 (2007). [https://doi.org/10.1016/S0021-9290\(07\)70280-4](https://doi.org/10.1016/S0021-9290(07)70280-4)
44. Pearcey, M.J., Bogduk, N.: Instantaneous axes of rotation of the lumbar intervertebral joints. *Spine* **13**, 1033–1041 (1988). <https://doi.org/10.1097/00007632-198809000-00011> (Phila. Pa. 1976)
45. Lemosse, D., Le Rue, O., Diop, A., Skalli, W., Marec, P., Lavaste, F.: Characterization of the mechanical behaviour parameters of the costo-vertebral joint. *Eur. Spine J.* **7**, 16–23 (1998). <https://doi.org/10.1007/s005860050021>
46. Duprey, S., Subit, D., Guillemot, H., Kent, R.W.: Biomechanical properties of the costovertebral joint. *Med. Eng. Phys.* **32**, 222–227 (2010). <https://doi.org/10.1016/j.medengphy.2009.12.001>
47. Beyer, B., Sholukha, V., Dugailly, P.M., Rooze, M., Moiseev, F., Feipel, V., Van Sint Jan, S.: In vivo thorax 3D modelling from costovertebral joint complex kinematics. *Clin. Biomech.* **29**, 434–438 (2014). <https://doi.org/10.1016/j.clinbiomech.2014.01.007>
48. Grellmann, W., Berghaus, A., Haberland, E.-J., Jamali, Y., Holweg, K., Reincke, K., Bierögel, C.: Determination of strength and deformation behavior of human cartilage for the definition of significant parameters. *J. Biomed. Mater. Res., Part A* **78A**, 168–174 (2006). <https://doi.org/10.1002/jbm.a.30625>
49. Mayer, O.H., Harris, J.A., Balasubramanian, S., Shah, S.A., Campbell, R.M.: A comprehensive review of thoracic deformity parameters in scoliosis. *Eur. Spine J.* **23**, 2594–2602 (2014). <https://doi.org/10.1007/s00586-014-3580-8>
50. Qiu, Y., Mao, S., Wang, B., Liu, Z., Zhu, F., Zhu, Z.: Clinical evaluation of the anterior chest wall deformity in thoracic adolescent idiopathic scoliosis. *Spine* **37**, E540–E548 (2011). <https://doi.org/10.1097/brs.0b013e31823a05e6> (Phila. Pa. 1976)
51. Kuklo, T.R., Potter, B.K., Lenke, L.G.: Vertebral rotation and thoracic torsion in adolescent idiopathic scoliosis. *J. Spinal Disord. Tech.* **18**, 139–147 (2005). <https://doi.org/10.1097/01.bsd.0000159033.89623.bc>

52. Takahashi, S., Suzuki, N., Asazuma, T., Kono, K., Ono, T., Toyama, Y.: Factors of thoracic cage deformity that affect pulmonary function in adolescent idiopathic thoracic scoliosis. *Spine* **32**, 106–112 (2007). <https://doi.org/10.1097/01.brs.0000251005.31255.25> (Phila. Pa. 1976)
53. Easwar, T.R., Hong, J.Y., Yang, J.H., Suh, S.W., Modi, H.N.: Does lateral vertebral translation correspond to Cobb angle and relate in the same way to axial vertebral rotation and rib hump index? A radiographic analysis on idiopathic scoliosis. *Eur. Spine J.* **20**, 1095–1105 (2011). <https://doi.org/10.1007/s00586-011-1702-0>
54. Oskouian, R.J., Shaffrey, C.I.: Degenerative lumbar scoliosis. *Neurosurg. Clin. N. Am.* **17**, 299–315 (2006). <https://doi.org/10.1016/j.nec.2006.05.002>
55. Vergari, C., Aubert, B., Lallemand-Dudek, P., Haen, T.X., Skalli, W.: A novel method of anatomical landmark selection for rib cage 3D reconstruction from biplanar radiography. *Comput. Methods Biomech. Biomed. Eng. Imaging Vis.* (2018). <https://doi.org/10.1080/21681163.2018.1537860>
56. Chi, W., Cheng, C., Yeh, W., Chuang, S., Chang, T., Chen, J.: Vertebral axial rotation measurement method. *Comput. Methods Programs Biomed.* **1**, 8–17 (2005). <https://doi.org/10.1016/j.cmpb.2005.10.004>
57. Mehta, M.H.: The rib-vertebra angle in the early diagnosis between resolving and progressive infantile scoliosis. *J. Bone Jt. Surg. Br.* **54-B**, 230–243 (1972). <https://doi.org/10.1302/0301-620X.54B2.230>
58. Sevastik, B., Xiong, B., Sevastik, J., Lindgren, U., Willers, U.: The rib vertebral angle asymmetry in idiopathic, neuromuscular and experimentally induced scoliosis. *Stud. Health Technol. Inform.* **37**, 107–110 (1997). <https://doi.org/10.3233/978-1-60750-881-6-107>
59. Lee, D.: Biomechanics of the thorax: a clinical model of in vivo function. *J. Man. Manip. Ther.* **1**, 13–21 (1993). <https://doi.org/10.1179/106698193791069771>